Heliyon 10 (2024) e28777

Contents lists available at ScienceDirect

Heliyon

journal homepage: www.cell.com/heliyon

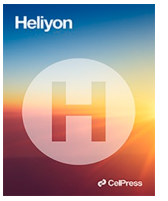

Research article

Optical characterization and dispersion analyses of plasma polymerized methyl acrylate thin films

S.D. Nath [a,b,*], A.H. Bhuiyan [b,c]

[a] Department of Physics, Khulna University of Engineering & Technology (KUET), Khulna 9203, Bangladesh
[b] Department of Physics, Bangladesh University of Engineering and Technology (BUET), Dhaka 1000, Bangladesh
[c] University of Information Technology and Sciences, Baridhara, Dhaka-1212, Bangladesh

ARTICLE INFO

Keywords:
Bandgap
Refractive index
Dielectric constant
Dispersion parameters
3rd order nonlinear susceptibility

ABSTRACT

This work reports the structural characteristics, surface morphology, linear and nonlinear optical properties of 110 to 225 nm thick plasma polymerized methyl acrylate (PPMA) thin films. X-ray diffraction analyses confirm the amorphous nature of the films. Field emission scanning electron micrographs of the films display cluster-based surface morphology. Attenuated total reflectance Fourier transform infrared spectroscopy confirms the chemical structural changes in the films. The optical properties were studied based on the absorbance, transmittance, and reflectance spectra measured by an ultraviolet–visible spectrophotometer within the wavelength ranges from 200 to 800 nm. The direct optical band gap and Urbach values are increased from 3.66 to 3.83 eV and 0.28 to 0.45 eV, respectively with increasing film thickness. The extinction coefficient and refractive index were evaluated, and discussed a correlation between the refractive index and the optical bandgap. The real and imaginary dielectric constants, volume/surface energy loss functions and skin depth were deduced. The oscillator energies and parameters were analyzed using the concept of Wemple-DiDomenico and Sellmeier models, respectively for a single oscillator. Static linear refractive index for the studied films exhibits normal dispersion behavior with film thicknesses and satisfied Moss, Ravindra-Gupta, and Herve-Vandamme rules. The linear susceptibility, third-order nonlinear susceptibility and the non-linear refractive index are considerably reduced from 0.20, 29.5×10^{-14} esu, and 5.89×10^{-12} esu with increasing optical band gap energies. The outcomes from the analyses of PPMA demonstrated their potential for usage in electronic, optoelectronic, and non-linear device applications.

1. Introduction

Plasma polymerization (PP) depicts a most convenient and versatile technique which has been used as a powerful tool over the past few decades. PP organic polymeric thin films have been recognized as one of the widely studied materials due to their outstanding physical and chemical properties [1,2]. The different characteristics of thin films depends on various parameters, such as monomer flow rate, discharge power, substrate temperature, and steady-state pressure in the reactor chamber [3,4]. The PP organic thin films have found extensive biocompatible applications in solar cells [5], gas and humidity sensors [6], transistors [7], and optical waveguides [8]. Organic devices are relatively more affordable and simpler to fabricate in comparison to their inorganic counterparts. PP

* Corresponding author. Department of Physics, Khulna University of Engineering & Technology (KUET), Khulna 9203, Bangladesh.
E-mail address: sumon.physics@phy.kuet.ac.bd (S.D. Nath).

https://doi.org/10.1016/j.heliyon.2024.e28777
Received 13 November 2023; Received in revised form 22 March 2024; Accepted 25 March 2024
Available online 27 March 2024

organic polymer films have attracted the attention of materials and solid state scientists who are keen to learn more about their structural, electrical, electronic and optical properties in order to develop high-quality polymer thin films utilizing a versatile technique for a range of significant applications. The special practical advantages of the PP technique are confirmative ultra-thin film fabrication, superior substrate adhesion, and chemically and physically viable surfaces [9]. It can be used to adhere thin films almost any substrates. Furthermore, while conventional polymer coating of a substrate necessitates multiple processes, PP completes all of them in practically one step [10]. Additionally, it may be used to create organic thin films from any volatile organic or organometallic molecule. Normally, light states are used for the deposition to reduce fragmentation modes. Most importantly, PP is environmentally friendly and has good deposition features which produce thin films that are homogeneous, biocompatible, and biodegradable and have special optoelectronic behaviours [11]. However, the disadvantages of the PP technique involve design complexity, necessitate certain fittings like expensive vacuum system, and cause unintended change of surface chemical composition. Moreover, determining the optimal conditions is time-consuming task due to the impact of process parameters on the chemical composition of the resultant polymer [12]. The significant techniques have been successfully utilized for synthesizing functional polymer thin films, including chemical vapor deposition [13], PP [14], spin/spray coating [15], atomic layer deposition [16], plasma enhanced chemical vapor deposition [17], sol gel [18], etc. The PP technique is strongly recommended since it can generate polymer thin films from almost any organic vapors and can fabricate thin films that cannot be made using other techniques. This process yields polymer thin films that are suitable for industrial usage. These films have exceptional mechanical, thermal, and chemical durability, are cross-linked and pinhole-free, and adhere well to almost all surfaces.

A large number of researchers have extensively studied PP thin polymer films in order to determine the morphological, thermal, structural, optical, and electrical properties to find their potential applications [19–23]. Hammani et al. [24] found values of the direct band gap energy (E_g^d) ranges from 3.8 to 4.1 eV for polymethylmethacrylate/polyethylene glycol polymer blends. El-naggar et al. [25] determined the E_g^d values for polymethyl methacrylate polymer between 4.46 and 4.52 eV. Haleshappa et al. [26] obtained the E_g^d values from 3.77 to 3.83 eV for methyl methacrylate thin films. Nasrin et al. [27] noted that PP n-butyl methacrylate thin films exhibited a smooth and pinhole-free surface and found E_g^d values between 3.64 and 3.80 eV. Hassanein et al. [28] found E_g^d values between 2.67 and 2.90 eV values for ZnSe thin films. Hassanein and Sharma [29] found the absorption coefficient values in the range of 10^4 cm^{-1} for $Cu_{25\text{-}x}(ZnGe)_{25\text{-}x}Se_{50+2x}$ thin films and they also determined the values of oscillator resonance energy (E_o) which increase from 2.939 to 3.422 eV, whereas the oscillator dispersion energy (E_d) values decrease from 30.831 to 24.342 eV. Park et al. [30] demonstrated that the surface morphology is largely homogeneous and amorphous in nature of PP methyl methacrylate utilizing attenuated total reflectance Fourier transform infrared (ATR-FTIR).

It is discerned from review of the past literature that the derivatives of methyl acrylate (MA) play a pivotal role in the field of science and technology. So, MA has been selected as the monomer precursor for the deposition of PPMA thin films. MA monomer is highly toxic through ingestion, inhalation, and skin absorption. If ventilation is insufficient in the laboratory, researchers must be used vapor-certified respirators, hand gloves, a lab coat, and splash goggles for safety during working with MA. But after plasma polymerization, MA becomes non-hazardous which is also environmentally friendly, biocompatible, and biodegradable [11].

The aim of this article is to prepare plasma polymerized methyl acrylate thin films samples of various thicknesses generated in a capacitively coupled plasma reactor operating at 22 W. Then comes the study and discuss the structural, optical, and dispersion parameters of PPMA thin films of various thicknesses. The X-ray diffraction analysis (XRD), FESEM, and ATR-FTIR were all used in this work to investigate the structural nature, surface morphology, and chemical bonding of PPMA thin films The ultraviolet visible (UV-VIS) spectroscopy were used to estimate thickness-dependent optical parameters such as direct band gap (E_g^d), linear refractive index (η), Urbach energy (E_U), real dielectric constants (ε_1) and imaginary dielectric constants (ε_2), quality factor (Q), the volume energy losses (VELF) and surface energy loss function (SELF), oscillator energy (E_o), dispersion energy (E_d), optical conductivity (σ_{opt}), skin depth (δ), reflection loss (RL), metallization parameter (M), optical surface resistance (R_s), high frequency and static dielectric constant, linear susceptibility ($\chi^{(1)}$) and 3rd order nonlinear susceptibility ($\chi^{(3)}$), the nonlinear refractive index (η'), are calculated and discussed in details. The optical properties of PPMA thin film could be controlled by altering both linear and nonlinear parameters as thickness is increased. These characteristics may reveal the suitability of PPMA for use in electronic and optoelectronic devices.

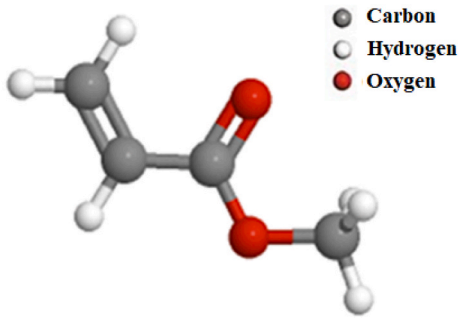

Fig. 1. Chemical structure of methyl acrylate.

2. Experimental

2.1. Thin film preparation on glass substrate

Transparent MA was purchased from VWR Inter. Ltd., BH15 1TD England and utilized exactly as it was delivered. The chemical structure of MA is shown in Fig. 1 while the general properties of MA are presented in Table 1. Before cutting to the proper size, the borosilicate glass substrates of dimensions 0.0254 m × 0.0762 m × 0.0012 m (Model: Sail Brand, China) which have strong chemical stability were first cleaned with a solution of detergent and water for the deposition of PPMA thin films. After that, an ultrasonic cleaner was utilized to fully clean the substrates. Then the substrates were rinsed in deionized water, and dried in a dryer. A cylindrical shaped plasma reactor chamber with two parallel stainless steel electrodes of thicknesses 0.001 m, placed parallel to one another, separated by a distance of about 0.039 m, serves as the setup for glow discharge polymerization. The entire setup is shown in Fig. 2 which consists of a vacuum pressure gauge, a pumping unit, a monomer injection system, an AC power supply (50 Hz) and a flow meter. A rotary pump was used to evacuate the glow discharge plasma reactor chamber. Over the capacitively coupled electrodes, the plasma glow discharge was produced. Glass substrates have been placed on the lower electrode after being cleaned and dried. A rotary pump was used to progressively lower the pressure within the reactor chamber to around 13.3 Pa. The plasma glow was created by applying electric power across the two parallel electrodes in the chamber. A tiny injection valve controlled the monomer flow rate (20 cm^3/min) to keep the working pressure steady throughout the deposition process. In the reactor, the monomer molecules were split up or fragmented before finally condensing onto the substrates. On the glass substrates, PPMA thin films were created for 45 to 90 min of deposition. The Fizeau interference technique was used to measure the thickness of the films. The following Eq. (1) was used to determine film thickness (d) [31]:

$$d = \frac{\lambda q}{2p} \tag{1}$$

; where λ is the wavelength of *Na* light = 589.3 nm, p is the fringe width and q is the step height which is the difference in height between two neighboring test surface sections of the fringe.

2.2. Devices and measurements

The structure of the PPMA thin films was examined by an X-ray diffractometer (XRD) (Model: Philips PW3040 X′Pert PRO, Germany) utilizing Cu-K_α as the target. The diffractometer reflections were taken at ambient temperature and the values of 2θ were swapped with a scan speed of 5° min^{-1} between 10° and 70° with step sampling of 0.02°. The accelerating voltage and current for the XRD machine were 40 kV and 30 mA, respectively. The incident X-ray wavelength is 1.541 Å.

A field emission scanning electron microscope (FESEM) (Model: 7600F, JEOL, JSM, Japan; resolution: 1 nm) was used to collect the surface morphological information of the thin films. To stop charging effects during FESEM, a small coating of platinum was also deposited onto the films using a platinum sputtering coater.

ATR-FTIR spectra of the PPMA thin film samples were acquired using a FTIR double-beam spectrophotometer (Model: FTIR Bruker Alpha, Germany).

The bandgap was also determined using information from UV–visible spectra obtained from a UV–Vis spectrophotometer (Model: UV-1601, SHIMADZU, Japan) at ambient temperature.

3. Results and discussion

3.1. XRD analysis

A representative of the XRD data of the PPMA thin films of thickness 200 nm is shown in Fig. 3, and it is clear that there are no clearly defined Bragg peaks in the XRD patterns which confirms the amorphous nature of the PPMA thin films. During plasma polymerization, the continual scattering of ions and electrons with the film surface may be the cause of the thin film's amorphous nature [32,33].

Table 1
General properties of methyl acrylate.

IUPAC name	Methyl acrylate
Molecular formula	$C_4H_6O_2$.
Purity	≥ 99.5%
Physical state	Colorless liquid
Molecular weight	86.09 g/mol
Density	0.95 g/cm^3
Boiling point	80 °C at 760 mm Hg
Refractive index	1.4021 (20 °C at 589 nm)

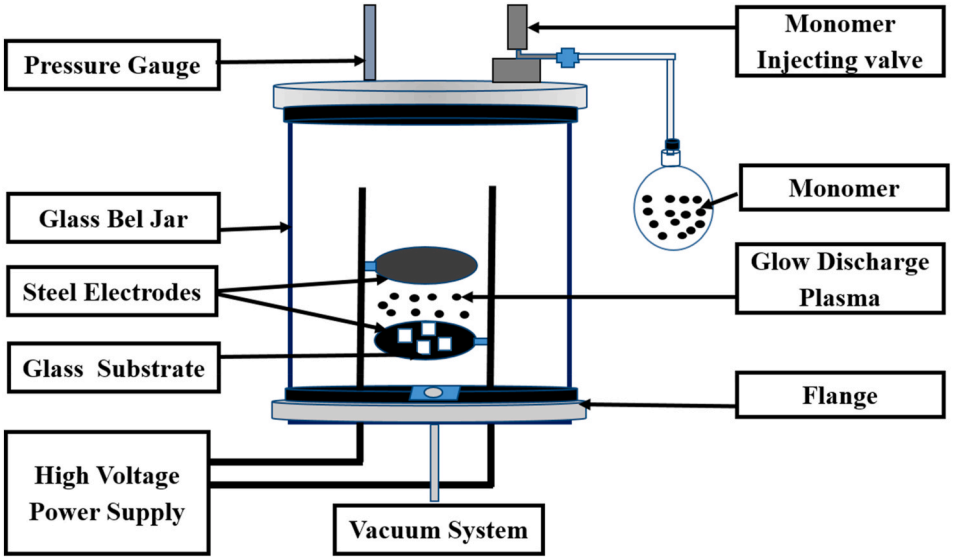

Fig. 2. The Schematic diagram PP system for fabrication of the PPMA thin films.

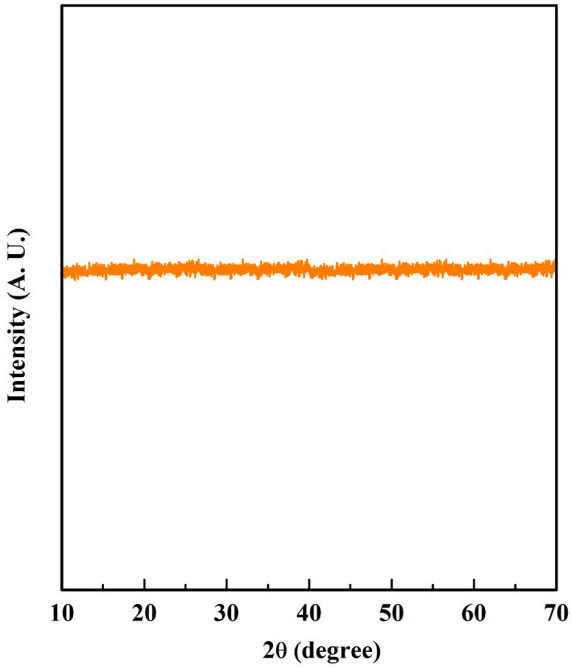

Fig. 3. A representative XRD pattern of the studied film of thickness 200 nm at 22 W.

3.2. Surface analyses

Fig. 4(a–d) displays the FESEM images of PPMA thin films of thickness 200 nm taken with magnification of × 30 k, × 50 k, × 100 k and × 150 k, respectively. At lower magnification, the surface of the PPMA thin films appear smooth and without any fractures. However, at higher magnification, a water wave-like structure becomes visible, suggesting the presence of aggregated portions within the films which is a result of prolonged polymerization and cross linking processes [34].

3.3. ATR-FTIR analyses

ATR-FTIR spectra shown in Fig. 5 reveal significant changes, demonstrating the fragmentation of MA structure owing to plasma

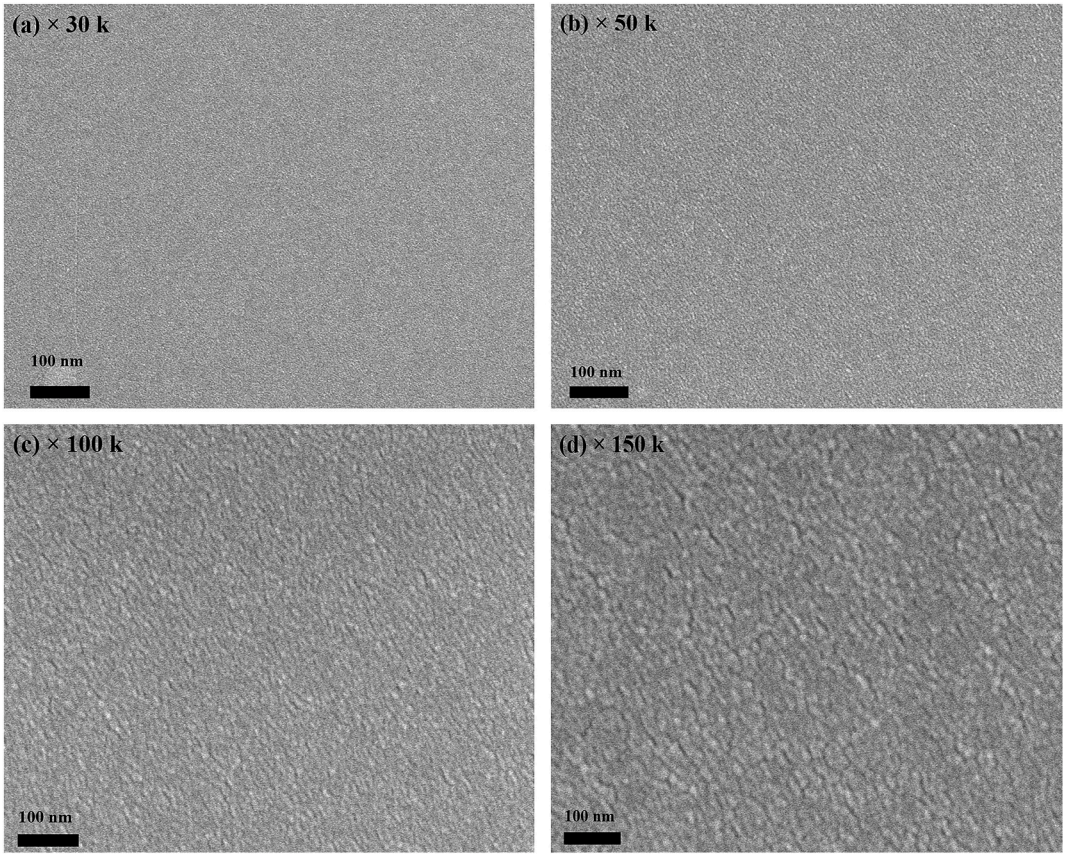

Fig. 4. The FESEM micrographs of the PPMA thin film of thickness 200 nm were taken with magnification of (a) × 30k, (b) × 50k, (c) × 100k and (d) × 150k at 22 W.

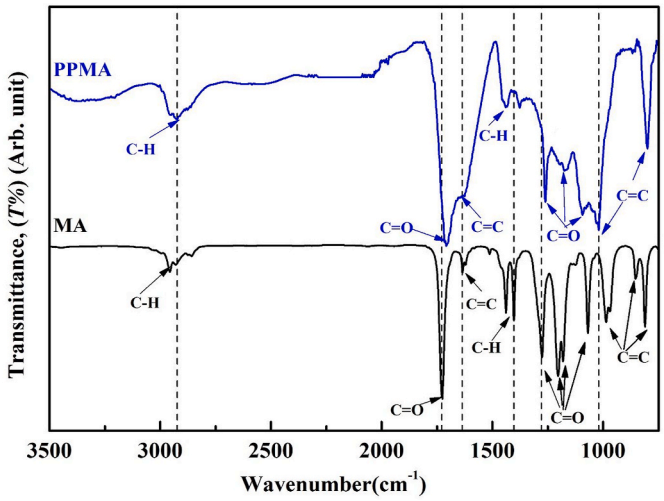

Fig. 5. ATR-FTIR spectra of the MA and studied films fabricated at 22 W.

polymerization. The types of vibrations corresponding to the absorption bands in the spectra are registered in Table 2. In the spectrum of PPMA, the relative absorption bands intensity is significantly decreased compared to MA. For PPMA and MA, the C–H stretching between 2800 and 3100 cm^{-1} is necessary for the methyl group to precisely identify the molecule as a molecular organic compound [35]. However, in the spectrum of PPMA, these bands appear as broad bands and are not detected due to very low intensity. The CH_2 stretching vibration are detected at 2917 and 2924 cm^{-1}, indicating the existence of these functional groups in both PPMA and MA

Table 2
ATR-FTIR vibration bands for MA and PPMA deposited at 22 W.

Assignment	Wavenumber (cm^{-1})	
	MA	PPMA Thin films
Stretching OH	–	3395
Stretching CH_3	2957	2957
Stretching CH_2	2917	2924
Stretching C–H	2856	Merged in broad band 2871
Stretching C═O	1727	1708
Stretching C═C	1635	1625
Bending CH_3	1439	1438
Bending CH_2	1403	1382
C–O	1069–1276	Merged in broad band 1094 - 1262
Bending C═C	811–987	Merged in broad band 802 - 1020

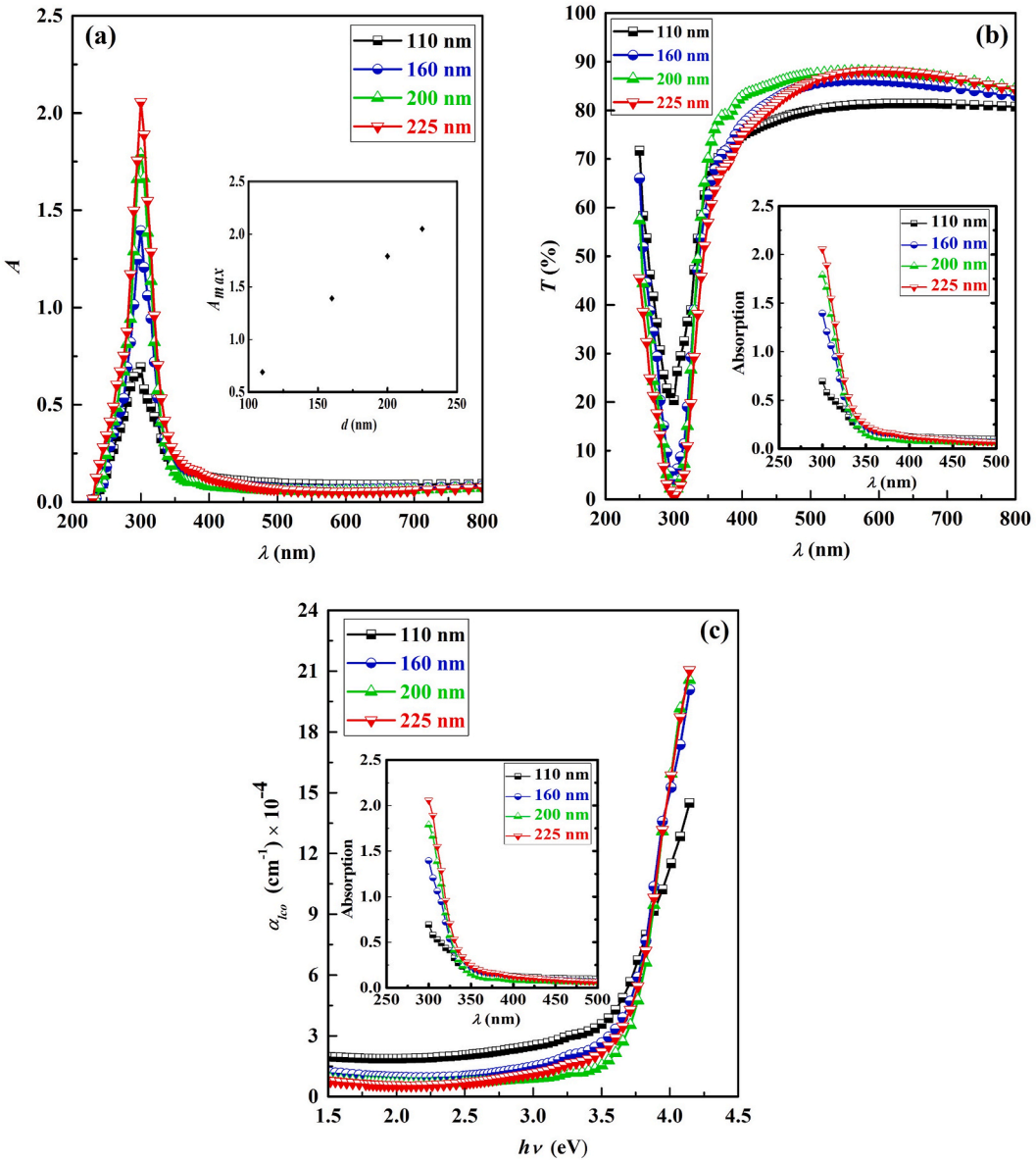

Fig. 6. Variation of (a) A with λ, (b) T with λ, and (c) α with $h\nu$ for the studied films at 22 W.

[36]. Absorption bands from 1617 to 1637 cm^{-1} in both PPMA and MA, represent C═C stretching vibrations. The absorption bands at 1439 for PPMA and 1438 cm^{-1} for MA are depicting the asymmetric CH_3 bending vibrations. The absorption peaks observed from 1382 to 1402 cm^{-1} of PPMA and MA, are attributed to CH_2 bending vibrations. In the case of PPMA, these peaks are shifted towards lower wavenumbers. This shift is caused by the hydrogen atoms being removed from the CH_3 [37]. The C–O and C═C bending vibrations are displayed from 800 to 1200 cm^{-1} [38]. Overall, the FTIR spectra of PPMA significantly differ from that of the MA, demonstrating that the presence of extremely energetic electrons and ions during plasma polymerization causes structural alterations and fragmentation of the monomer.

3.4. Optical properties

3.4.1. Absorbance, transmittance and linear absorption co-efficient

The UV–Visible absorbance (A) and optical transmittance (T) spectra of PPMA films of thicknesses 110, 160, 200, and 225 nm were investigated at ambient temperature and are depicted in Fig. 6a and b, respectively. An interesting observation in the absorption spectra is the sharp rise of A in shorter wavelengths, reaching a maximum at around 301 nm for various film thicknesses, with the UV zone experiencing the highest absorption. Beyond this point, as the wavelength increases, the A for all of the PPMA thin films quickly begins to decrease up to around 375 nm. The A drops at a slower pace beyond 375 nm, with the UV zone experiencing the highest absorption. The minor shift in the wavelength at which the highest A occurs with film thickness, as shown in Table 3, is an important feature. This change is a result of the conjugated system in PPMA becoming more prevalent [39].

Correspondingly, the FTIR spectra reveal the appearance of a C═C band in the range of 1625–1635 cm^{-1}, which serves as an indication of an expanding conjugated π-system. This observation further supports the notion of increased conjugation within the PPMA thin films. Regarding the T spectra (Fig. 6b), it is evident that the T increases with longer wavelengths up to 425 nm for various thicknesses. Beyond this point, the T reaches a nearly constant value. PPMA films of different thicknesses are translucent and display an 80 to 90% high T in the visible range. Between 110 and 225 nm, the A increases in the visible range while T displays opposite patterns of these films. The inset Fig. 6b illustrates, the absorption edge's position is dependent on the thickness of the thin films and has been moved to lower wavelengths.

At room temperature, the linear absorption co-efficient (α_{lco}) in terms of absorbance (A) and thickness (d) for PPMA films was evaluated using the following Eq. (2) [40,41]:

$$\alpha_{lco} = 2.303 \frac{A}{d} \tag{2}$$

Analyzing Fig. 6c, it can be observed that the values of α_{lco} start increasing at approximately 3.0 eV. Beyond 3.5 eV, this increase becomes more rapid. The optical linear absorption coefficient (α_{lco}) is nearly visible and has high values in between 10^4 and 10^5 cm^{-1}. The inset Fig. 6c illustrates, the absorption edge's position has been moved to lower wavelengths with increasing film thicknesses. The existence of several optical transitions inside PPMA is confirmed by the nonlinear character of each curve. Additionally, the exponential edge seen in the absorption spectra indicates the existence of defects in the PPMA thin films.

3.4.2. Optical bandgap calculation

Optical band gap is one of the crucial parameters associated with the electronic structure [42]. There is a significant amount of absorption in the thin films because the incoming photons have sufficient energy to drive electrons into the conduction band from the valence band. This straightforward approach reveals the position of the optical absorption edge and clarifies the band structure of the film's characteristics. Using this approach, the optical absorption edge was discovered. The following Eq. (3) known as Tauc's technique was utilized to conduct an investigation into the optical absorption edge [43,44]:

$$\alpha_{lco} h\nu = B\left(h\nu - E_g\right)^m \tag{3}$$

; where B = proportionality factor or band-tailing parameter which depends on the type of the electronic transition, and E_g = optical band gap. Exponent 'm' is dependent on the nature of transition which determines electronic transition type in the gap. It has various values, such as $m = 1/2$ (allowed direct), $m = 2$ (allowed indirect), $m = 3/2$ (forbidden direct) and $m = 1/3$ (forbidden indirect) transitions. The following Eq. (4) is a representation of Eq. (3) [45].

Table 3
Linear optical parameter of the studied films of various d at 22 W.

Parameters	Thickness, d			
	110 nm	160 nm	200 nm	225 nm
λ_{max} (nm)	299	300	301	301
A_{max}	0.69	1.39	1.79	2.05
E_g^d (eV)	3.66	3.79	3.82	3.83
E_U (eV)	0.45	0.34	0.28	0.31
σ_s	0.057	0.076	0.092	0.083
$E_{e\text{-}p}$	11.7	8.82	7.26	8.04

$$\frac{d\left[ln\left(\alpha_{pco}h\nu\right)\right]}{d(h\nu)} = \frac{m}{h\nu - E_g} \tag{4}$$

The plot of d[ln($\alpha_{lco}h\nu$)]/d($h\nu$) against $h\nu$ that is delineated in Fig. 7a, displays a break or discontinuity that was noticed at the point from equation (4). The discontinuity is appeared at a specific energy, $E_g = 3.27$ eV. Based on the slope of the ln($\alpha_{lco}h\nu$) versus ln($h\nu$ - Eg) curves shown in Fig. 7b, it is discovered that the value of m is about 1/2. Therefore, it appears from the observed value of m that the allowed direct transitions produce the fundamental edge of absorption inside the films. During the transition phase, the integrity of the total momentum and energy of the photon-electron system must be maintained. The plot of $(\alpha_{lco}h\nu)^2$ versus $h\,\nu$ for different d of PPMA is shown in Fig. 7c. The E_g^d values are varied from 3.66 to 3.83 eV with d at 22 W that are tabulated in Table 3 and found to have a slightly lower direct band gap value by comparing with previous research at 35 W for PPMA [46]. The amorphous nature of these films is confirmed by the computed optical band values, which rise with increasing d. The thin films can be utilized as an insulating material in a nonvolatile organic digital memory because their band gaps can be easily tuned by changing the thicknesses [47]. When a photon is absorbed by an electron at the valence band edge, the electron becomes excited and moves toward the bottom of the conduction band.

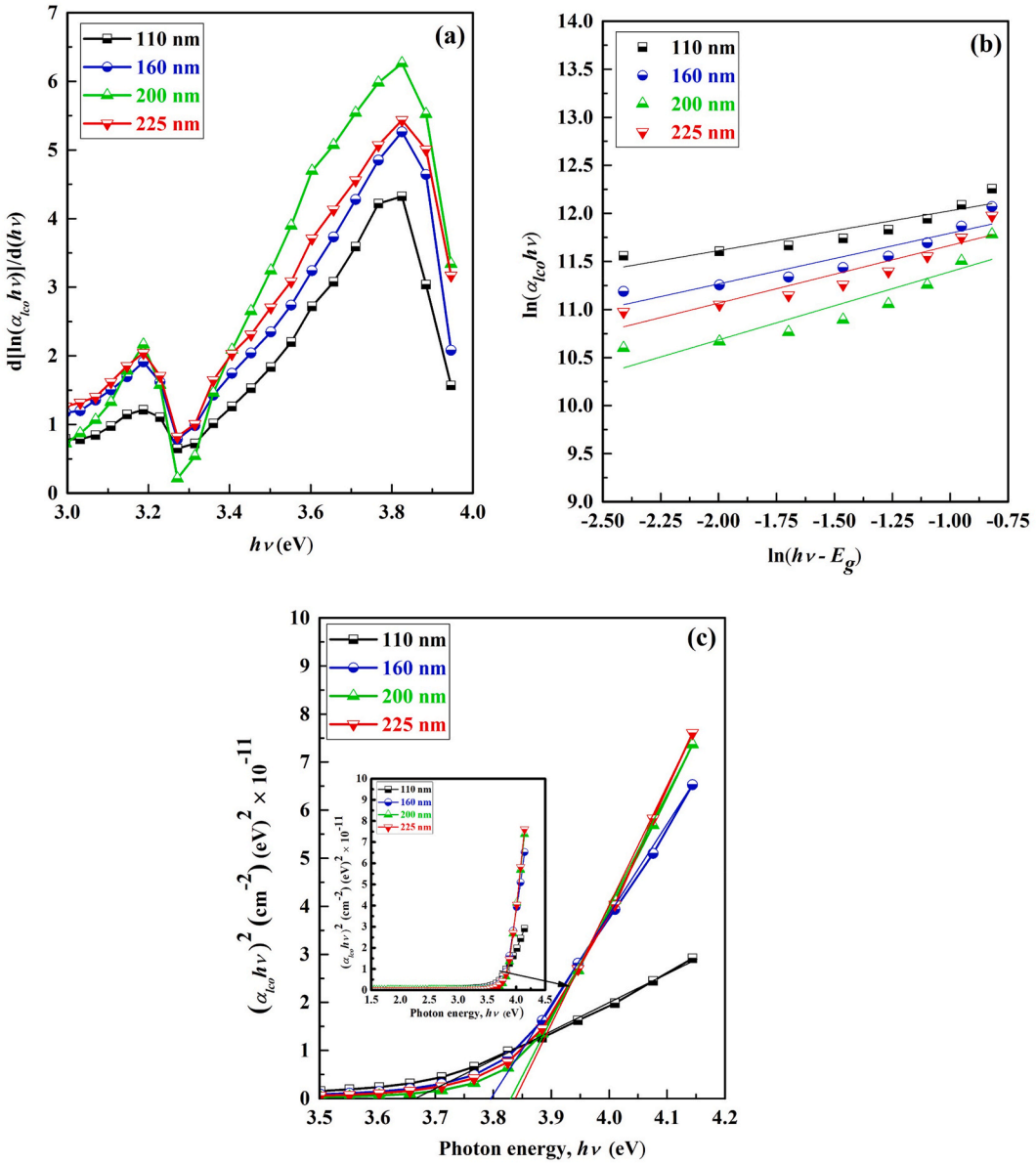

Fig. 7. (a) d[ln($\alpha_{lco}h\nu$)]/d($h\nu$) against $h\nu$ (b) ln($\alpha_{lco}h\nu$) versus ln($h\nu$ - Eg) and (c) $(\alpha_{lco}h\nu)^2$ versus $h\nu$ curves for the studied films at 22 W.

3.4.3. Urbach energy, extinction co-efficient, and refractive index

The Urbach tail indicates the defect levels exist inside the forbidden gap. The Urbach energy (E_U) was calculated using Eq. (5) [48]:

$$E_U = \left[\frac{d(h\nu)}{d(ln\alpha_{lco})}\right] \tag{5}$$

Fig. 8a illustrates the $ln\alpha_{lco}$ versus $h\nu$ curves for PPMA films of different d. The values of E_U ranges from 0.28 to 0.45 eV are calculated and tabulated in Table 3. Because the structural disorders are decreasing in the band gap, the E_U values decrease as film thickness increases up to 200 nm, then it increases.

The steepness parameter ($\sigma_s = k_BT/E_U$) indicates the broadening in the optical absorption edge because of electrons-phonon interaction. The σ_s values have been calculated considering T = 298 K and k_B = Boltzmann's constant = 1.38×10^{-23} JK^{-1} and are listed in Table 3. The observed lower values of σ_s demonstrate a lower rate of phonon-electron scattering and a narrower optical absorption edge due to lower density of states close to the optical absorption edge [49].

Electron-phonon interaction ($E_{e\text{-}p}$= $2/3\sigma_s$) indicates an interaction strength between electrons and phonons. The value of $E_{e\text{-}p}$ exhibits the opposite relationship of the σ_s and the results are tabulated in Table 3. This knowledge may be helpful for a variety of applications, including optoelectronics and solar cell technologies. The $E_{e\text{-}p}$ values suggests a broadening of the filled energy bands of PPMA films that vary in thickness from 110 to 200 nm whereas for 225 nm, $E_{e\text{-}p}$ value is decreased which points to a reduction of the

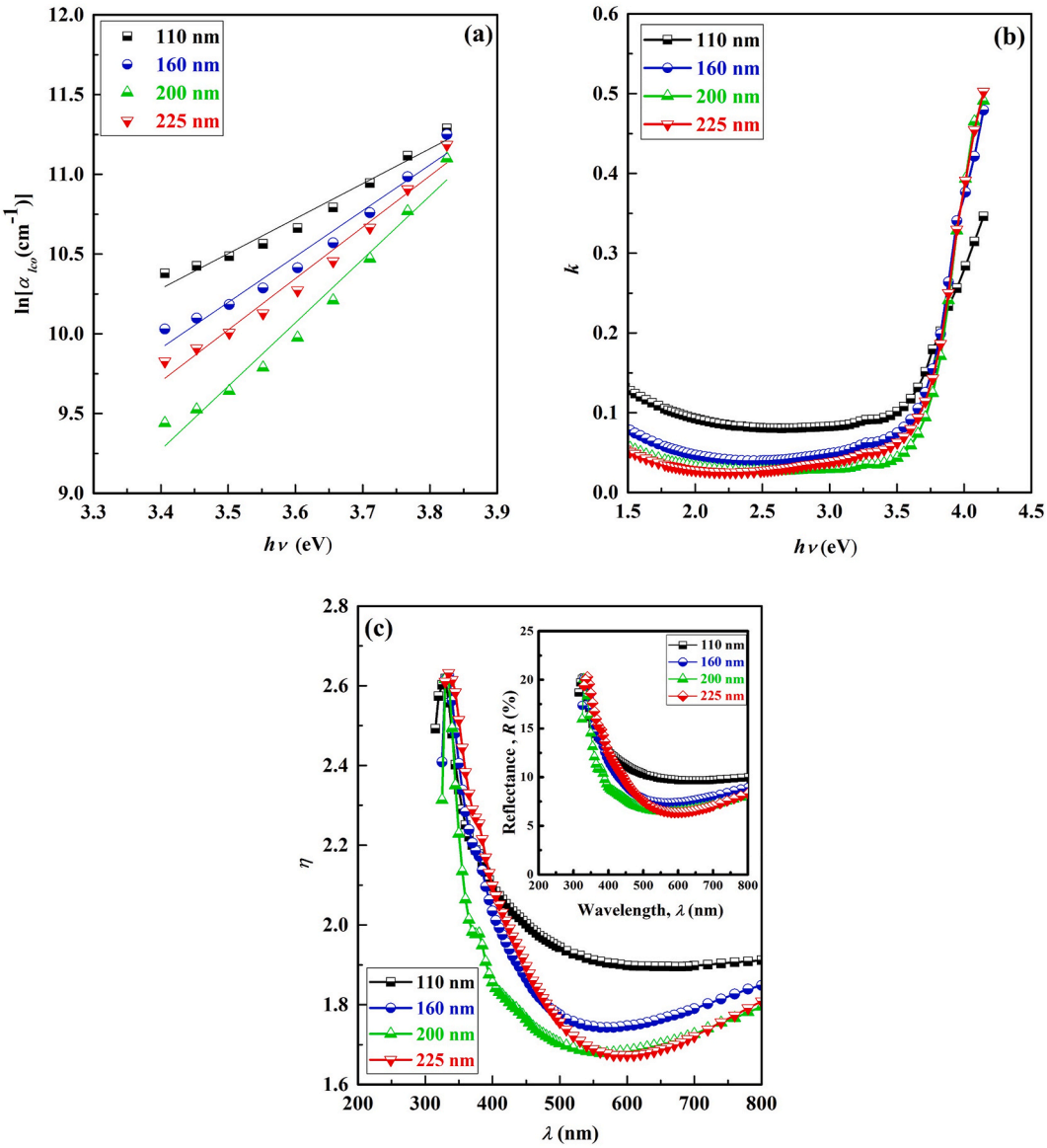

Fig. 8. The plots of (a) $ln\alpha$ vs $h\nu$, (b) k vs $h\nu$, and (c) η vs λ of the studied films at 22 W.

filled energy bands expansion according to the strong binding approximation [50].

The extinction co-efficient (k) indicates the polarization ability of the material. The k can be obtained using α with the assistance of Eq. (6) [51].

$$k = \frac{\alpha\lambda}{4\pi} \tag{6}$$

The relationship between k and $h\nu$ is shown in Fig. 8b. With increasing $h\nu$, the value of k increases, possibly indicating a reduction in electron transmission across the mobility gap. The linear refractive index (η) provides information on how light moves through a material. The following Fresnel's formula in Eq. (7) was used to compute η [52]:

$$\eta = \left(\frac{1+R}{1-R}\right) + \sqrt{\frac{4R}{(1-R)^2} - k^2} \tag{7}$$

Fig. 8c exhibits η at various λ, depicting the normal dispersion behavior of the PPMA films of various d. The value of η is larger in the lower wavelength regime, whereas in the wavelength regime ($300\ nm \leq \lambda \leq 550\ nm$), it decreases drastically. However, above this photon wavelength, η has no significant variation. For high film thickness, η is lower. Greater changes in the direction of light within the films are caused by a higher η which suggests slower light travel. As a result, the optical intensities rise which making the material more effective and useful for non-linear interactions [53,54].

The η displays normal dispersion behavior which satisfies the Moss relation [55], Ravindra and Gupta relation [56] and Herve and Vandamme relation [57]. In addition, this theoretical models are adequate for materials with a bandgap greater than 1.4 eV [58,59]. The η values of the films were also calculated from the E_g^d values using the following Eqs. (8)–(10), respectively.

$$\eta(Moss) = \left(\frac{95}{E_g^d}\right)^{\frac{1}{4}} eV \tag{8}$$

$$\eta(RG) = 4.084 - 0.62\, E_g^d \tag{9}$$

$$\eta(HV) = \sqrt{1 + \left(\frac{A'}{E_g^d + B'}\right)^2} \tag{10}$$

;where $A' = -13.6$ eV = the ionization energy of hydrogen and $B' = 3.47$ eV. The $\eta_{max}(Vis)$ values are listed in Table 4. The $\eta_{max}(Vis)$ values are almost independent of d. According to Table 4, η (Moss), η (RG) and η (HV) values are decreased with increasing d as well as E_g^d. This trend indicates that PPMA thin films allow light to pass more freely through and have less absorbing nature in the vis-NIR region [60].

Table 4
Optical dispersive parameter of the studied films of various d at 22 W.

Dispersive parameters	Thickness, d			
	110 nm	160 nm	200 nm	225 nm
$\eta_{max}(Vis)$	2.62	2.63	2.62	2.63
$\eta\ (Moss)$	2.26	2.24	2.23	2.22
$\eta\ (RG)$	1.81	1.73	1.72	1.71
$\eta\ (HV)$	2.15	2.12	2.11	2.10
$\varepsilon_\infty\ (Moss)$	5.09	5.01	4.99	4.98
$\varepsilon_\infty\ (RG)$	3.29	3.01	2.94	2.92
$\varepsilon_\infty\ (HV)$	4.64	4.51	4.48	4.47
ε_∞ (Adachi)	6.06	5.88	5.84	5.82
ε_0 (Adachi)	7.25	6.85	6.75	6.72
E_g^d (eV)	3.66	3.79	3.82	3.83
E_0 (eV)	*6.9*	*7.38*	*7.13*	*6.99*
E_d (eV)	17.7	14.19	12.39	11.45
E_0/E_g^d	1.90	1.95	1.87	1.83
η_0	1.89	1.71	1.65	1.62
ε_∞	3.56	2.92	2.74	2.64
$f = E_0E_d$	122.13	104.72	88.34	80.04
n_{opt}	1.92	1.97	1.98	1.99
M_{-1}	2.57	1.92	1.74	1.64
M_{-3}	0.0539	0.0353	0.0342	0.0335
λ_0 (nm)	304	342	287	424
S_0 (m^{-2})	2.93×10^{13}	1.75×10^{13}	2.25×10^{13}	1.13×10^{13}

3.4.4. Dielectric constants, quality factor, SELF and VELF

The complex dielectric constants (ε^*), real dielectric constants (ε_1) and imaginary dielectric constants (ε_2) were calculated utilizing the following Eqs. (11)–(13), respectively [61,62]:

$$\varepsilon^* = \varepsilon_1 + i\varepsilon_2 = (\eta + ik)^2 \tag{11}$$

where

$$\varepsilon_1 = \eta^2 - k^2 \tag{12}$$

and

$$\varepsilon_2 = 2\eta k \tag{13}$$

The ε_1 describes the de-acceleration of a light wave as it travels through the film material for any damped oscillator. As a result, it links to the energy contained in the substance and explains how electromagnetic waves disperse. On the other hand, the ε_2 indicates how much energy is received or lost in light. It is therefore regarded as a damping factor as it has to do with the energy lost and

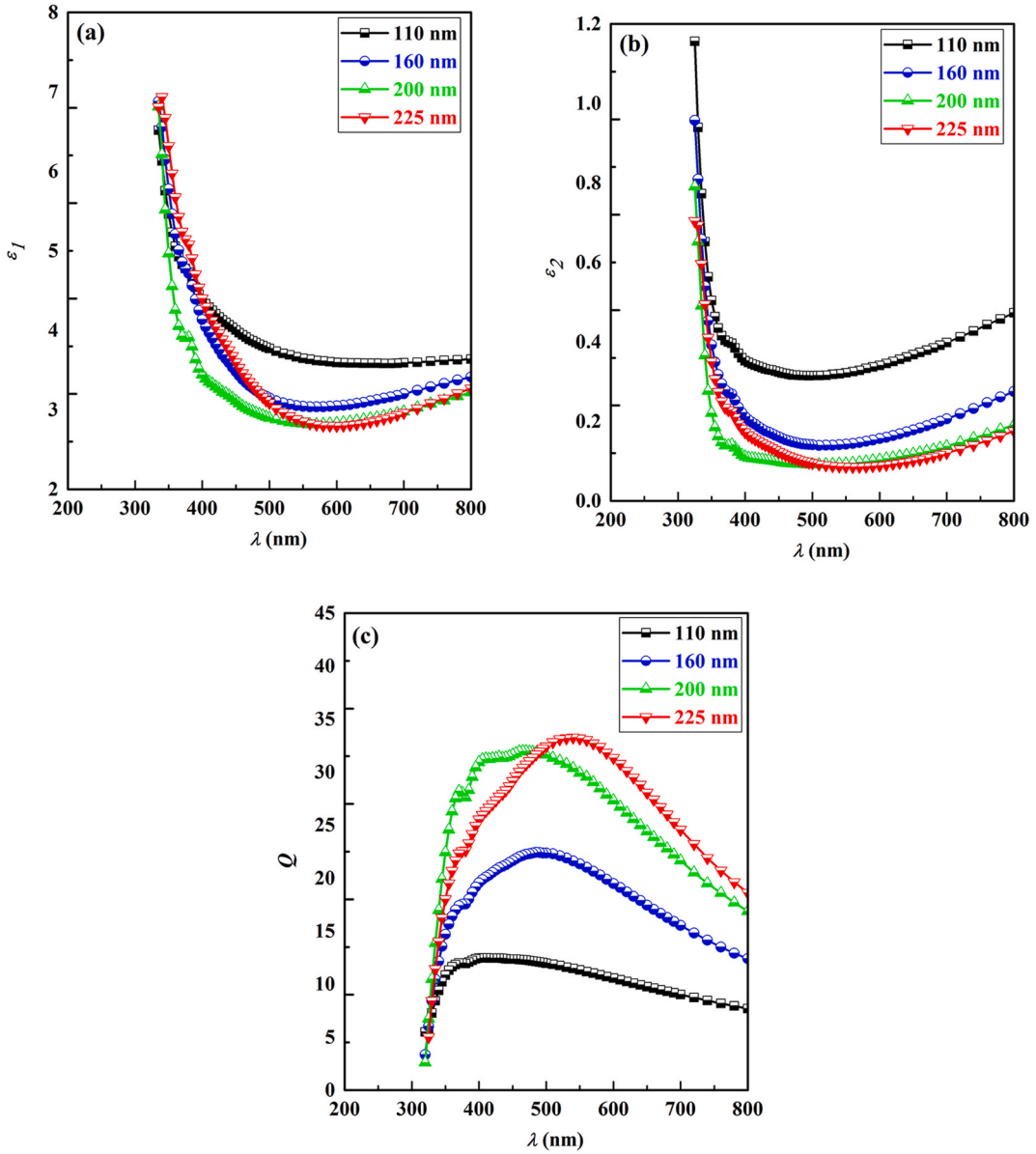

Fig. 9. The variations of (a) ε_1 and (b) ε_2 and (c) Q as a function of λ for the studied films at 22 W.

dissipated within the material when the light wave passes. Thus, numerous dielectric characteristics, including the dielectric loss factor, the quality factor, the volume and surface energy loss functions, and optical conductivity, etc., may be inferred from the known values of the dielectric constant [63]. From Fig. 9a and b, it is noted that the values of ε_1 is more than ε_2 for all these films of various thicknesses because ε_1 are highly dependent on the refractive index (η) where $\eta \gg k$ whereas ε_2 is only depends on k values where small k values decreases the product of n and k. Initially ε_1 and ε_2 dramatically decreased up to wavelength 550 nm and then no significant changes are observed. The variation of the dielectric constants with the incident photon energy indicates that there are some interactions have occurred between free electrons and incident photons in the wavelength range from 300 nm to 550 nm.

The dielectric loss tangent ($tan\ \delta$) describes how an incoming electromagnetic radiation's energy or amplitude is reduced as it passes through the film medium. The ratio between the imaginary dielectric constant (ε_2) and real dielectric constant (ε_1) is known $tan\ \delta$. The inverse of $tan\ \delta$ is called the quality factor (Q).

The $tan\ \delta$ and Q were calculated with the assistance of Eqs. (14) and (15), respectively [64,65]:

$$tan\ \delta = \frac{\varepsilon_2}{\varepsilon_1} \tag{14}$$

and

$$Q = \frac{1}{tan\ \delta} = \frac{\varepsilon_1}{\varepsilon_2} \tag{15}$$

Fig. 9c depicts the relationship between Q of PPMA films and the change in wavelength for various d. In comparison to the high and medium wavelength regions, the Q values are observed to be lower at lower wavelengths. The Q values are also observed to drastically decrease up to 800 nm as the d rises. Additionally, the Q values increase as d increase. The Q values for each of the investigated films decrease significantly in the high wavelength area. In comparison to lower thicknesses, films of higher thicknesses are more effective [66].

The surface (SELF) and volume (VELF) energy loss functions were utilized to determine the probability of energy which is caused by the rapidly moving electron inside the materials. The oscillation is dependent on the SELF and VELF. It is suggested that the activation of plasma oscillations in the ocean of conduction electrons is responsible for this loss. The values of ε_2 and ε_1 are used to determine surface energy losses. The SELF and VELF were calculated using Eqs. (16) and (17), respectively [67,68].

$$SELF = \frac{\varepsilon_1}{\left[(\varepsilon_1 + 1)^2 + \varepsilon_2^2\right]} \tag{16}$$

$$VELF = \frac{\varepsilon_2}{(\varepsilon_1^2 + \varepsilon_2^2)} \tag{17}$$

The spectral behavior of the SELF is depicted in Fig. 10a. It is noted that in the lower λ region ($300\ nm \leq \lambda \leq 550\ nm$), the SELF values are increased dramatically but above the λ region, the values are almost saturated. The behavior of the VELF is depicted in Fig. 10b along with the λ, which decreases with increasing the d. The SELF are greater than VELF for PPMA films of various d. Increases in SELF with d increases may be caused by an increase in disorder or defects, which results in an increase in the carrier's collisions

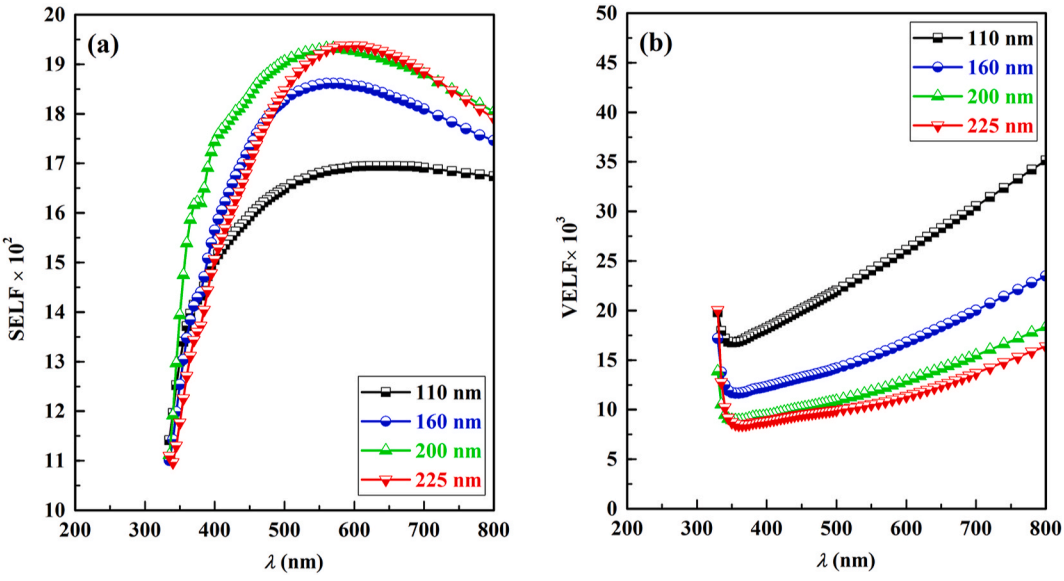

Fig. 10. Variation of (a) SELF with λ and (b) VELF with λ for the studied films at 22 W.

while traveling through the material. Thus, the optical conductivity may be responsible for the variations in the values of the VELF and SELF loss functions [69].

3.4.5. Optical conductivity and skin depth

The optical conductivity , σ_{opt} is a powerful optical parameter for implementing the optical response as well as electronic state of the thin films. The following Eq. (18) in terms of the speed of light (c) was used to evaluate the σ_{opt} of PPMA thin films [70]:

$$\sigma_{opt} = \frac{\alpha_{lco}\eta c}{4\pi} \tag{18}$$

The values of σ_{opt} are seen to significantly fall notably up to 550 nm wavelength in PPMA thin films. Beyond this limit, as the thin films interact with light photons, the σ_{opt} values remain almost constant and decrease toward zero as seen in Fig. 11a. Further, it could be noted that for thicker PPMA films, the σ_{opt}, values are lower. This variation between σ_{opt} and d is thought to be the result of localized states forming at PPMA thin film defect sites [71,72].

Skin effect is measured using skin depth (δ) metric, which measures how well incident photons penetrate a medium. The following Eq. (19) was used to examine how the k depends on the δ [73]:

$$\delta = \frac{\lambda}{2\pi k} \tag{19}$$

The spectrum of δ versus $h\nu$ of the PPMA films is shown in Fig. 11 b. At the lower energy region ranges between 2 and 2.5 eV, the δ values are very larger for various d but with increasing energy, it drops dramatically and nearly independent of d. The δ values are large in the lower energy range indicates that there are more electron collisions in this region [74].

3.4.6. Dispersive energy parameters

A thorough physical explanation of the examined parameters is provided by the single effective oscillator model. The Wemple-DiDomenico relationship in Eq. (20) was used to explain the dispersion analysis of η [75,76]:

$$\eta^2 = 1 + \frac{E_0 E_d}{{E_0}^2 - E^2} \quad Or, \left(\eta^2 - 1\right)^{-1} = \frac{E_0}{E_d} - \frac{E^2}{E_0 E_d} \tag{20}$$

;where E_d is the dispersion energy, E $(=h\nu)$ is the photon energy, and E_0 is the oscillator energy. Fig. 12a displays a plot of the $(\eta^2-1)^{-1}$ against $(h\nu)^2$ for PPMA films of various d results in a straight line that cuts the Y-axis in the upward direction. The slope of this straight line is equal to $(E_o E_d)^{-1}$, and its intersection provides the ratio between E_o and E_d. The calculated E_o and E_d values are listed in Table 4 that are fluctuating with d. According to Tanaka [77,78], E_o is nearly equal to two times of E_g^d. For validation of these results, the values of the ratio $\frac{E_o}{E_g^d}$ for PPMA thin films were calculated and obtained results are fit in with the Tanaka relationship which are listed in Table 4. The obtained results are quite reasonably support the Tanaka relationship. The fluctuation of E_o may be related to variations in the number of scattering centers with respect to PPMA thin film thicknesses.

According to Maxwell relation [79], the theoretical high frequency dielectric constants, ε_∞ of PPMA films of various d were computed with the assistant of Eq. (21) using η *(Moss)*, η *(RG)*, and η *(HV)* values:

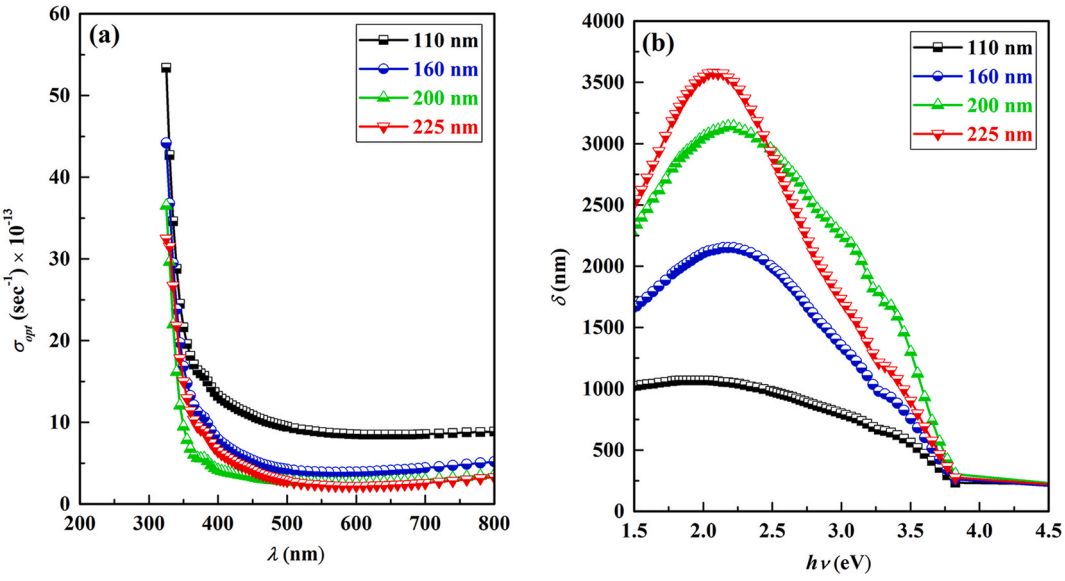

Fig. 11. Variation of (a) σ_{opt} with λ and (b) δ, with $h\nu$ for the studied films at 22 W.

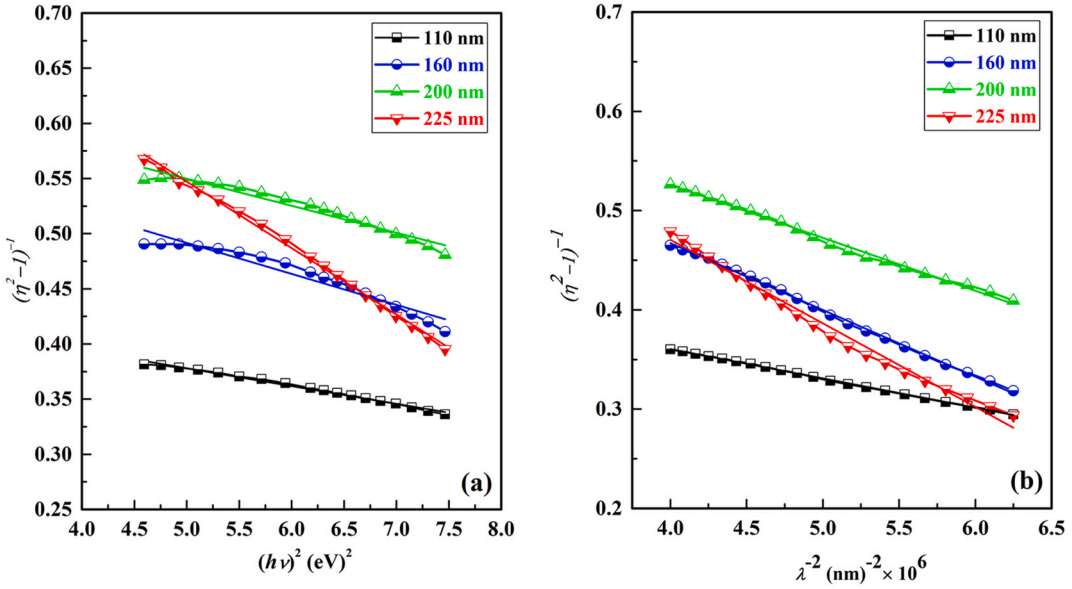

Fig. 12. (a) $(\eta^2-1)^{-1}$ *vs* $(h\nu)^2$ and (b) $(\eta^2-1)^{-1}$ *vs* λ^{-2} of the studied films at 22 W.

$$\varepsilon_\infty = \eta^2 \tag{21}$$

Adachi proposed the theoretical formula for evaluating both the high frequency dielectric constants, ε_∞ and static dielectric constants, ε_0. The ε_∞ and ε_0 values were calculated using Eqs. (22) and (23), respectively [80]:

$$\varepsilon_\infty = 11.26 - 1.42\, E_g^d \tag{22}$$

$$\varepsilon_0 = 18.52 - 3.08\, E_g^d \tag{23}$$

Table 4 shows that ε_∞ *(Moss),* ε_∞ *(RG),* ε_∞ *(HV),* ε_∞ (Adachi) and ε_0 (Adachi) values signify decreasing trends with increasing *d*.

The values of E_o and E_d were computed from the $(\eta^2-1)^{-1}$ against $(h\nu)^2$ plot in Fig. 12a. So, the experimental high frequency dielectric constant (ε_∞) and static refractive index (η_0) were calculated using the following Eq. (24) and tabulated in Table 4 [81]:

$$\varepsilon_\infty = 1 + \frac{E_d}{E_0},\ \eta_0 = \sqrt{\varepsilon_\infty} \tag{24}$$

The ε_∞ values is correlated with the ε_∞ *(Moss),* ε_∞ *(RG),* ε_∞ *(HV),* ε_∞ (Adachi) and ε_0 (Adachi) values where ε_∞ values are decreased with increasing *d* of PPMA films. It can be said that increasing thickness will help reduce the power loss in the PPMA thin films and increase the suitability of the material for high frequency and power device applications [82].

The first order moments of spectra $\left(M_{-1} = \frac{E_d}{E_0}\right)$ and third ($M_{-3} = \frac{M_{-1}}{E_0^2}$) order moments of spectra are computed which are tabulated in Table 4. The obtained M_{-1} and M_{-3} values are decreased with increasing *d* of the PPMA films. The oscillator strength ($f = E_0E_d$) of the material decreased with increasing *d* that are shown in Table 4.

The optical electronegativity (n_{opt}) values were computed using the following Eq. (25) [83]:

$$n_{opt} = \left(\frac{C}{\eta_0}\right)^{\frac{1}{4}} \tag{25}$$

;where C = 25.54. The calculated values of n_{opt} are increased with increasing *d* that are tabulated in Table 4. The optical electronegativity influences the non-linear parameters because of n_{opt} is correlated with the static refractive index.

The values of both wavelength (λ_0) and the average strength of the oscillator (S_0) were obtained from the plot of $(\eta^2-1)^{-1}$ against λ^{-2} according to the following Sellmeier's dispersion Eq. (26) [84]:

$$(\eta^2-1)^{-1} = \frac{1}{S_0\lambda_0^2} - \frac{1}{S_0\lambda^2} \tag{26}$$

In Fig. 12b–a straight line can be drawn with a slope of $\left(\frac{1}{S_0}\right)$ and an intersection with the Y-axis at a value equal to $(S_0\lambda_0^2)^{-1}$. Consequently, the λ_0 and S_0 values are determined which are tabulated in Table 4.

3.4.7. Reflection loss, mettalization parameter, and optical surface resistance

The reflection loss (*RL*) of PPMA films of different *d* were computed utilizing Eq. (27) in terms of linear refractive index (η) [85]:

$$RL = \frac{\eta^2 - 1}{\eta^2 + 2} \tag{27}$$

The fluctuation of the RL with increasing *d* of PPMA thin films is shown in Fig. 13a. There are certain losses in electromagnetic wave strength when light travels through thin coatings. The propagation velocity is reduced as a result of these losses. This rise in the reflection loss values is likely caused by an increase in the *k* values and SELF and VELF, which demonstrate an increase in scattering, losses, and absorption.

Metallization parameter, *M* denotes the insulating or metallic properties of the materials which was calculated using the following Eq. (28) [86]:

$$M = 1 - \frac{(\eta^2 - 1)}{(\eta^2 + 2)} = 1 - RL \tag{28}$$

If $M > 1$, the materials' metallic nature is confirmed, and if $M < 1$, the studied samples' non-metallic behavior is indicated. Fig. 13b displays the *M*-values, which range between 0.3 and 0.7 for PPMA films of various *d*. It has been noted that the obtained *M* values of the current film samples are less than unity and more than zero, indicating that PPMA films are insulating materials.

The Kirchhoff's functions are the resistance of the thin film's surface that results from the excitation of electrons by photons striking the surface. The estimated static refractive index, η_0 was utilized to compute the optical surface resistance (R_s) using the following Eq. (29) [87,88]:

$$R_s = \frac{-4\pi}{c} \times \frac{1}{\eta_0 \, ln(T)} \tag{29}$$

The R_s values are increased with increasing *d* shown in Fig. 13c. The photon wavelength and *d* rise with an increase in Kirchhoff's functions.

3.4.8. Non-linear optical properties

Nonlinear optical properties of the substance were also investigated to better understand the nonlinear properties of PPMA films that are essential for utilization in device applications, notably in optoelectronics [89]. The linear susceptibility ($\chi^{(1)}$) and 3rd order nonlinear susceptibility ($\chi^{(3)}$) and the non-linear refractive index (η') which connected with the static refractive index (η_0) were computed using the following Eqs. (30)–(32), respectively [90–92]:

$$x^{(1)} = \frac{\eta_0^2 - 1}{4\pi} \tag{30}$$

$$x^{(3)} = K \left[x^{(1)}\right]^4 \tag{31}$$

; where C = constant = 1.7×10^{-10} esu

$$\eta' = \frac{12\pi x^{(3)}}{\eta_0} \tag{32}$$

The calculated values of $\chi^{(1)}$, $\chi^{(3)}$ *and* η' are listed in Table 5. The values of $\chi^{(1)}$, $\chi^{(3)}$ and η' are 0.20, 29.5×10^{-14} esu, and 5.89×10^{-12} esu are decreased with increasing *d*. $\chi^{(3)}$ is a crucial indicator of a material's structural symmetry and provides details on the strength of the chemical bonds forming between the thin film's molecules. High $\chi^{(3)}$ has advantages for several prospective applications, including frequency converters, switching devices, and electro-optic modulators [93].

4. Conclusions

Plasma polymerized methyl acrylate thin films has been generated using glow discharge plasma polymerization technique. A water wave-like structure becomes visible at higher magnification which suggesting the existence of aggregated portions within the films. The new absorption peak in PPMA spectrum suggests monomer fragmentation during plasma polymerization. The obtained absorption coefficient values ranges from 10^4 to 10^5 cm^{-1} for all *d*. The direct band gap (E_g^d) and Urbach energy (E_U) values are increased from 3.66 to 3.83 eV and from 0.28 to 0.45 eV, respectively with increasing *d*. X-ray diffraction analyses (XRD) analysis, metallization parameters and high value of E_g^d confirms the dielectric nature of the films. The real dielectric constant is much greater than the imaginary dielectric constant ($\varepsilon_1 \gg \varepsilon_2$) which confirms that polymeric material responses to light falling on it. The higher quality factor (*Q*) values are observed for the 225 nm that means thicker films are more effective than thinner for device applications. Theoretical high frequency dielectric constants (ε_∞) values are fitted with the ε_∞ (Moss), ε_∞ (RG), ε_∞ (HV), ε_∞ (Adachi) and ε_0 (Adachi) values where ε_∞ values are decreased with increasing *d*. The electronic transition occurs for the variations in the values of the surface energy loss function (SELF) and volume energy loss function (VELF). The skin depth (δ) fluctuates with *d* that indicates more electron

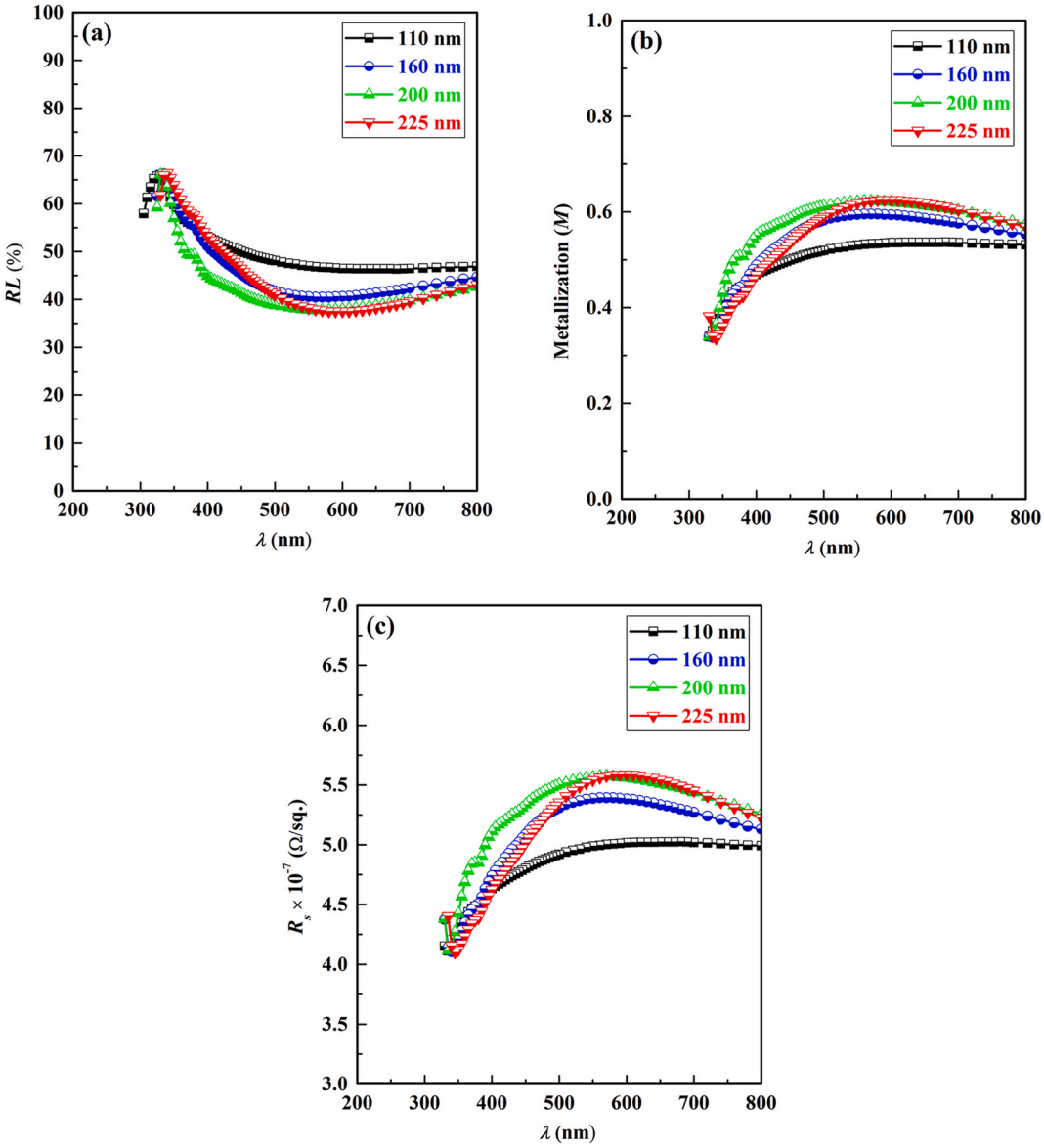

Fig. 13. Variation of (a) *RL* with λ, (b) *M* with λ, and (c) R_s with λ, for the studied films at 22 W.

Table 5
Non-linear optical parameters of the studied films of various *d* at 22 W.

Parameters	Thickness, *d*			
	110 nm	160 nm	200 nm	225 nm
$x^{(1)}$	0.20	0.15	0.14	0.13
$x^{(3)}$ (esu)	29.5×10^{-14}	9.32×10^{-14}	6.22×10^{-14}	4.91×10^{-14}
$\eta^{'}$ (esu)	5.89×10^{-12}	2.05×10^{-12}	1.42×10^{-12}	1.14×10^{-12}

collisions at lower energy range, but it becomes very low and independent of *d* in the higher energy range. The obtained dispersion energies (E_d) values ranges from 11.45 to 17.7 eV and the oscillator energies (E_0) values ranges from 6.90 to 7.38 eV. The estimated values of the optical electronegativity (n_{opt}) are slightly increased from 1.92 to 1.99 while the third-order nonlinear susceptibility ($\chi^{(3)}$) of PPMA thin films decreased from 29.5×10^{-14} esu to 4.91×10^{-14} esu by increasing *d*. The PPMA thin films is a suitable candidates for optoelectronic, electronics device and non-linear optics.

Data availability statement

Data will be made available on request.

CRediT authorship contribution statement

S.D. Nath: Writing – original draft, Visualization, Software, Methodology, Investigation, Conceptualization. **A.H. Bhuiyan:** Writing – review & editing, Supervision, Resources.

Declaration of competing interest

The authors declare that they have no known competing financial interests or personal relationships that could have appeared to influence the work reported in this paper.

Acknowledgements

Financial grant sanctioned by the BUET authority to pursue this work is thankfully acknowledged. S. D. Nath is grateful to the authority of KUET for granting him permission to conduct this research.

References

[1] K.W. Lu, H.L. Chen, H.P. Chen, C.C. Kuo, Design of organic/inorganic multilayer water vapor barrier thin films deposited via plasma polymerization for encapsulation, Thin Solid Films 767 (2023) 139672, https://doi.org/10.1016/j.tsf.2023.139672.
[2] T. Dufour, From basics to frontiers: a comprehensive review of plasma-modified and plasma-synthesized polymer films, Polymers 15 (17) (2023) 3607, https://doi.org/10.3390/polym15173607.
[3] P. Mandracci, P. Rivolo, Recent advances in the plasma-assisted synthesis of silicon-based thin films and nanostructures, Coatings 13 (6) (2023) 1075, https://doi.org/10.3390/coatings13061075.
[4] J. Zhang, T. Bai, W. Liu, M. Li, Q. Zang, C. Ye, J.Z. Sun, Y. Shi, J. Ling, A. Qin, B.Z. Tang, All-organic polymeric materials with high refractive index and excellent transparency, Nat. Commun. 14 (2023) 3524, https://doi.org/10.1038/s41467-023-39125-w.
[5] D. Zhang, W. Yu, L. Zhang, X. Hao, Progress in the synthesis and application of transparent conducting film of AZO (ZnO:Al), Materials 16 (16) (2023) 5537, https://doi.org/10.3390/ma16165537.
[6] R. Amri, Z.B. Hamed, D. Gamra, M. Lejeune, H. Bouchriha, Correction to: optical modeling and investigation of thin films based on plasma-polymerized HMDSO under oxygen flow deposited by PECVD, J. Mater. Sci. Mater. Electron. 34 (20) (2023) 1544, https://doi.org/10.1007/s10854-023-10981-y.
[7] M.S.A. Kamel, M. Oelgemöller, M.V. Jacob, Sustainable plasma polymer encapsulation materials for organic solar cells, J. Mater. Chem. A 10 (2022) 4683–4694, https://doi.org/10.1039/D1TA10608B.
[8] K. Wu, Y. Yu, Z. Hou, X. Guan, H. Zhao, S. Liu, T. Zhang, A humidity sensor based on ionic liquid modified metal organic frameworks for low humidity detection, Sensor. Actuator. B Chem. 355 (2022) 131136, https://doi.org/10.1016/j.snb.2021.131136.
[9] H. Kabir, M.M. Rahman, K.M. Uddin, A.H. Bhuiyan, Structural, morphological, compositional and optical studies of plasma polymerized 2-furaldehyde amorphous thin films, Appl. Surf. Sci. 423 (2017) 983–994, https://doi.org/10.1016/j.apsusc.2017.06.284.
[10] N. Mehta, Chapter 1, "Overview of coating deposition techniques,", in: S. Ahmed, V.S. Dakre (Eds.), Tribology and Characterization of Surface Coatings, Wiley-Scrivener, 2022, pp. 1–32, https://doi.org/10.1002/9781119818878.ch1. ISBN13: 9781119818861.
[11] N. Banu, A.H. Bhuiyan, K.S. Hossain, Characterization of structural and optical properties of plasma polymerized diethanolamine thin films, Adv. Polym. Technol. 37 (8) (2018) 3084–3094, https://doi.org/10.1002/adv.22079.
[12] L.L. Haidar, M. Baldry, S.T. Fraser, B.B. Boumelhem, A.D. Gilmour, Z. Liu, Z. Zheng, M.M.M. Bilek, B. Akhavan, Surface-active plasma-polymerized nanoparticles for multifunctional diagnostic, targeting, and therapeutic probes, ACS Appl. Nano Mater. 5 (12) (2022) 17576–17591, https://doi.org/10.1021/acsanm.2c03213.
[13] A. Khlyustova, Y. Cheng, R. Yang, Vapor-deposited functional polymer thin films in biological applications, J. Mater. Chem. B 8 (31) (2020) 6588–6609, https://doi.org/10.1039/D0TB00681E.
[14] C. Ma, A. Nikiforov, D. Hegemann, N.D. Geyter, R. Morent, K, K. Ostrikov, Plasma-controlled surface wettability: recent advances and future applications, Int. Mater. Rev. 68 (1) (2023) 2047420, https://doi.org/10.1080/09506608.2022.2047420.
[15] Y. Kim, J. Kim, J.W. Han, J. Choi, Multiscale mechanics of yttria film formation during plasma spray coating, Appl. Sur. Sci. 572 (2022) 151416, https://doi.org/10.1016/j.apsusc.2021.151416.
[16] J.L. Wree, D. Rogalla, A. Ostendorf, K.D. Schierbaum, A. Devi, Plasma-enhanced atomic layer deposition of molybdenum oxide thin films at low temperatures for hydrogen gas sensing, ACS Appl. Mater. Interfaces 15 (11) (2023) 14502–14512, https://doi.org/10.1021/acsami.2c19827.
[17] E.Z. Frątczak, J. Balcerzak, M. Rogala, Optoelectronic properties of cold plasma-deposited, oxidized Sn–C thin films, Materials 17 (2) (2024) 314, https://doi.org/10.3390/ma17020314.
[18] H. Li, Y. Hu, S. Wei, Y. Meng, N. Wang, Q. Zhang, L. Liu, B. Peng, Oxygen plasma-assisted ultra-low temperature sol-gel-preparation of the PZT thin films, Ceram. Inter. 49 (7) (2023) 10864–10870, https://doi.org/10.1016/j.ceramint.2022.11.279.
[19] R. Nasrin, M.J. Rahman, A.H. Bhuiyan, Schottky conduction mechanism in plasma polymerized N-benzylaniline thin films, Thin Solid Films 792 (2024) 140251, https://doi.org/10.1016/j.tsf.2024.140251.
[20] V. Mazánková, P. Sťahel, P. Matoušková, A. Brablec, J. Čech, L. Prokeš, V. Buršíková, M. Stupavská, M. Lehocký, K. Ozaltin, P. Humpolíček, D. Trunec, Atmospheric pressure plasma polymerized 2-ethyl-2-oxazoline based thin films for biomedical purposes, Polymers 12 (2020) 2679, https://doi.org/10.3390/polym12112679.
[21] D.A. Zuza, V.O. Nekhoroshev, A.V. Batrakov, A.B. Markov, I.A. Kurzina, Characterization of hexamethyldisiloxane plasma polymerization in a DC glow discharge in an argon flow, Vacuum 207 (2023) 111690, https://doi.org/10.1016/j.vacuum.2022.111690.
[22] S.D. Nath, A.H. Bhuiyan, Charge carrier transport mechanism in plasma polymerized methyl acrylate thin films, Thin Solid Films 786 (2023), https://doi.org/10.1016/j.tsf.2023.140098.
[23] S. Muramoto, D.J. Graham, D.G. Castner, ToF-SIMS analysis of ultrathin films and their fragmentation patterns, J. Vac. Sci. Technol. A 42 (2) (2024) 023416, https://doi.org/10.1116/6.0003249.
[24] S. Hammani, S. Daikhi, M. Bechelany, A. Barhoum, Role of ZnO, nanoparticles loading in modifying the morphological, optical, and thermal properties of immiscible polymer (PMMA/PEG) blends, Materials 15 (23) (2022) 8453, https://doi.org/10.3390/ma15238453.
[25] A.M. El-naggar, A.M. Kamal, A.M. Aldhafiri, Effect of $NiFe_2O_4$-$ZnMn_2O_4$ mixture on the structural, optical and dielectric characteristics of PMMA/PEO blends, J. Macromol. Sci. B (2023) 2253696, https://doi.org/10.1080/00222348.2023.2253696.

[26] D. Haleshappa, R. Bairy, Shridevi, S.N. Kakathkar, H. Vijeth, N. Gummagol, Thiophene-centered PMMA unified thin films with electrical, photoluminescence, and third-order nonlinear optical potentials for optoelectronic applications, Mater. Today Commun. 35 (2023) 106052, https://doi.org/10.1016/j.mtcomm.2023.106052.

[27] R. Nasrin, K.S. Hossain, A.H. Bhuiyan, Morphological, elemental, and optical characterization of plasma polymerized *n*-butyl methacrylate thin films, Appl. Phys. A 124 (5) (2018) 1–8, https://doi.org/10.1007/s00339-018-1795-y.

[28] A.S. Hassanien, K.A. Aly, A.A. Akl, Study of optical properties of thermally evaporated ZnSe thin films annealed at different pulsed laser powers, J. Alloys Comp. 685 15 (2016) 733–742, https://doi.org/10.1016/j.jallcom.2016.06.180.

[29] A.S. Hassanien, I. Sharma, Synthesis, analysis, and characterization of structural and optical properties of thermally evaporated chalcogenide a-Cu-Zn-Ge-Se thin films, Mater. Chem. Phys. 311 (2024) 128524, https://doi.org/10.1016/j.matchemphys.2023.128524.

[30] C.S. Park, E. Jung, H. Jang, G. Bae, Shin, H.S. Tae, Synthesis and properties of plasma-polymerized methyl methacrylate via the atmospheric pressure plasma polymerization technique, Polymers 11 (3) (2019) 396, https://doi.org/10.3390/polym11030396.

[31] S. Tolansky, The measurement of thin film thickness by interferometry, J. Opt. Soc. Am. 41 (6) (1951) 425–426, https://doi.org/10.1364/JOSA.41.000425.

[32] S.A. Gad, H. Shaban, B.A. Mansour, G.M. Mahmoud, Determination and analysis of linear and nonlinear optical properties and electrical conductivity of amorphous $Pb_xGe_{42-x}Se_{48}Te_{10}$ thin films, Appl. Phys. A 126 (2020) 354, https://doi.org/10.1007/s00339-020-3449-0.

[33] R. Nasrin, M.J. Rahman, A.T.M.K. Jamil, K.S. Hossain, A.H. Bhuiyan, Thickness dependent structural and surface properties of plasma polymerized N-benzylaniline thin films, Appl. Phys. A 127 (2021) 240, https://doi.org/10.1007/s00339-021-04326-x.

[34] H. Kaczmarek, Changes to polymer morphology caused by u.v. irradiation: 1. Surface damage, Polymer 37 (2) (1996) 189–194, https://doi.org/10.1016/0032-3861(96)81086-X.

[35] S.M. Palardonio, M.R. Vasquez Jr., Deposition and morphology of direct current plasma-polymerized aniline, J. Vac .Sci. Technol. B 41 (3) (2023) 034201, https://doi.org/10.1116/6.0002497.

[36] R.T. Colney, Infrared Spectroscopy, Allyn and Bacon Inc., Boston, 1975.

[37] C.N. Banwell, E.M. McCash, Fundamentals for Molecular Spectroscopy, fourth ed., McGraw-Hill, London, 1994.

[38] P.R. Griffiths, Fourier transform infrared spectrometry, Science 222 (1983) 297–302, https://doi.org/10.1126/science.6623077.

[39] S. Sheikh, J. Sarder, A.H. Bhuiyan, J. Rahman, Structural and optical behaviours of methyl acrylate-vinyl acetate composite thin films synthesized under dynamic low-pressure plasma, Heliyon 9 (8) (2023) e18524, https://doi.org/10.1016/j.heliyon.2023.e18524.

[40] F.M. Amin, A.M. El-Mahalawy, K.T. Abdel-Salam, M. Abdel-Salam, Structural and optical exploration of promising zinc (8-hydroxyquinoline) thin films for wide-scale optoelectronic applications, Opt. Mater. 139 (2023) 113754, https://doi.org/10.1016/j.optmat.2023.113754.

[41] L.F. Nassier, M.H. Shinen, Study of the optical properties of poly (methyl methacrylate) (PMMA) by using spin coating method, Mater. Today Proce. 60 (3) (2022) 1660–1664, https://doi.org/10.1016/j.matpr.2021.12.213.

[42] A.A. Bani-Salameh, A.A. Ahmad, A.M. Alsaad, I.A. Qattan, I.A. Aljarrah, Synthesis, optical, chemical and thermal characterizations of PMMA-PS/CeO_2 nanoparticles thin film, Polymers 13 (7) (2021) 1158, https://doi.org/10.3390/polym13071158.

[43] J. Tauc, in: Optical Properties of Amorphous Semiconductors, Springer, 1974, https://doi.org/10.1007/978-1-4615-8705-7_4.

[44] A.S. Hassanien, Intensive linear and nonlinear optical studies of thermally evaporated amorphous thin Cu-Ge-Se-Te films, J. Non-Cryst. Solids 586 (2022), https://doi.org/10.1016/j.jnoncrysol.2022.121563.

[45] F.A. Tuma, M.T. Obeed, A.A. Jari, H.A. Badran, T.A. Alaridhee, Effect of gamma ray on self-induced diffraction patterns of organic compound Poly (methyl-methacrylate films), Results Phys. 52 (2023) 106858, https://doi.org/10.1016/j.rinp.2023.106858.

[46] S.D. Nath, A.H. Bhuiyan, Surface morphology and optical properties of thin films of plasma polymerized methyl acrylate, Opt. Mater. 136 (2023) 113474, https://doi.org/10.1016/j.optmat.2023.113474.

[47] R. Nasrin, M.J. Rahman, A.T.M.K. Jamil, A.H. Bhuiyan, Thickness dependent thermal and optical properties of plasma polymerized *N*-benzylaniline thin films, Mole. Cryst. Liq. Cryst. 738 (1) (2022) 50–66, https://doi.org/10.1080/15421406.2021.2017103.

[48] F. Urbach, The long-wavelength edge of photographic sensitivity and of the electronic absorption of solids, Phys. Rev. 92 (1953) 1324, https://doi.org/10.1103/PhysRev.92.1324.

[49] F.O. Efe, B. Olofinjana, O. Fasakin, M.A. Eleruja, E.O.B. Ajayi, Compositional, structural, morphological, optical and electrical property evolutions in MOCVD Cu-Zn-S thin films prepared at different temperatures using a single solid source precursor, J. Electron. Mater. 48 (2019) 8000–8013, https://doi.org/10.1007/s11664-019-07636-2.

[50] A.A. Ahmad, Q.M. Al-Bataineh, A.M. Alsaad, T.O. Samara, K.A. Al-izzy, Optical properties of hydrophobic ZnO nano-structure based on antireflective coatings of ZnO/TiO2/SiO2 thin films, Physi. B Cond. Mat. 593 (2020) 412263, https://doi.org/10.1016/j.physb.2020.412263.

[51] C. Emir, A. Tataroglu, E. Coşkun, S.B. Ocak, Structural and optical properties of interfacial InSe thin film, ACS Omega 9 (7) (2024) 7588–7596, https://doi.org/10.1021/acsomega.3c06600.

[52] A.S. Hassanien, S. Ishu, S. Pankaj, Inference of Sn addition on optical properties of the novel thermally evaporated thin a-Ge15Te50S35-xSnx films and some physical properties of their glasses, Mater. Chem. Phys. 293 (2023) 126887, https://doi.org/10.1016/j.matchemphys.2022.126887.

[53] S. Giri, P. Priyadarshini, D. Alagarasan, R. Ganesan, R. Naik, Annealing-induced phase transformation in $In_{10}Se_{70}Te_{20}$ thin films and its structural, optical and morphological changes for optoelectronic applications, RSC Adv. 13 (2023) 24955, https://doi.org/10.1039/D3RA03731B.

[54] I. Sharma, S.K. Tripathi, P.B. Barman, Effect of Bi addition on the optical behavior of a-Ge-Se-In-Bi thin films, Appl. Surf. Sci. 255 (2008) 2791–2795, https://doi.org/10.1016/j.apsusc.2008.08.011.

[55] T.S. Moss, Photoconductivity in the elements, Proc. Phys. Soc. 64 (6) (1951) 590, https://doi.org/10.1088/0370-1298/64/6/113.

[56] N.M. Ravindra, P. Ganapathy, J. Choi, Energy gap–refractive index relations in semiconductors-An overview, Infr. Phys. Techn. 50 (1) (2007) 21–29, https://doi.org/10.1016/j.infrared.2006.04.001.

[57] P.J.L. Herve, L.K.J. Vandamme, General relation between refractive index and energy gap in semiconductors, Infra. Phy. Techn. 35 (1994) 609–615, https://doi.org/10.1016/1350-4495(94)90026-4.

[58] A.M. Shakra, I.S. Yahia, S.S. Shenouda, Determination of the refractive index of indigo dye thin film/flexible polyacetate substrate, Opt. Quan. Elec. 55 (2023) 823, https://doi.org/10.1007/s11082-023-05014-1.

[59] S.K. Tripathy, Refractive indices of semiconductors from energy gaps, Opt. Mater. 46 (2015) 240–246, https://doi.org/10.1016/j.optmat.2015.04.026.

[60] P. Priyadarshini, S. Das, D. Alagarasan, R. Ganesan, S. Varadharajaperumal, S. Sahoo, R. Naik, The impact of fluence dependent proton ion irradiation on the structural and optical properties of $Bi_5In_{30}Se_{65}$ thin films for nonlinear optical devices, RSC Adv. 12 (2022) 5012–5026, https://doi.org/10.1039/D2RA00097K.

[61] F. Abeles, Optical Properties of Solids, North-Holland Publishing Company, Amsterdam, London, New York, 1972 044410058X. American Elsevier.

[62] J.B. Kana Kana, J.M. Ndjaka, G. Vignaud, A. Gibaud, M. Maaza, Thermally tunable optical constants of vanadium dioxide thin films measured by spectroscopic ellipsometry, Optics Comm 284 (3) (2011) 807–812, https://doi.org/10.1016/j.optcom.2010.10.009.

[63] A.S. Hassanien, Studies on dielectric properties, opto-electrical parameters and electronic polarizability of thermally evaporated amorphous Cd50S50−xSex thin films, J. Alloy. Comp. 671 (2016) 566–578, https://doi.org/10.1016/j.jallcom.2016.02.126.

[64] F. Yakuphanoglu, A. Cukurovali, İ. Yilmaz, Determination and analysis of the dispersive optical constants of some organic thin films, Physica B: Cond. Matter 351 (1–2) (2004) 53–58, https://doi.org/10.1016/j.physb.2004.05.010.

[65] A.S. Hassanien, I. Sharma, Dielectric properties, Optoelectrical parameters and electronic polarizability of thermally evaporated a-Pb-Se-Ge thin films, Physica B: Cond. Matt. 622 (2021) 413330, https://doi.org/10.1016/j.physb.2021.413330.

[66] A.S. Hassanien, I. Sharma, K.A. Aly, Linear and nonlinear optical studies of thermally evaporated chalcogenide a-Pb-Se-Ge thin films, Physica B: Cond. Matt. 613 (2021), https://doi.org/10.1016/j.physb.2021.412985.

[67] F. Yubero, V.M. Jiménez, A.R. González-Elipe, Optical properties and electronic transitions of SnO_2 thin films by reflection electron energy loss spectroscopy, Surf. Sci. 400 (1–3) (1998) 116–126, https://doi.org/10.1016/S0039-6028(97)00854-6.

[68] P. Sharma, M.S. El-Bana, S.S. Fouad, V. Sharma, Effect of compositional dependence on physical and optical parameters of Te17Se83−xBix glassy system, J. Alloy. Comp. 667 (2016) 204–210, https://doi.org/10.1016/j.jallcom.2016.01.179.
[69] S.S. Fouad, I.M. El Radaf, P. Sharma, M.S. El-Bana, Multifunctional CZTS thin films: structural, optoelectrical, electrical and photovoltaic properties, J. Alloy. Compd. 757 (2018) 124–133, https://doi.org/10.1016/j.jallcom.2018.05.033.
[70] J.N. Zemel, J.D. Jensen, R.B. Schoolar, Electrical and optical properties of epitaxial films of PbS, PbSe, PbTe, and SnTe, Phys. Rev. 140 (1965) 330, https://doi.org/10.1103/PhysRev.140.A330.
[71] H. Mahr, Ultraviolet absorption of KI diluted in KCl crystals, Phys. Rev. 125 (1962) 1510, https://doi.org/10.1103/PhysRev.125.1510.
[72] J.F. Eloy, Power Lasers, vol. 59, John Wiley & Sons, France, 1984.
[73] P.W. Gilberd, The anomalous skin effect and the optical properties of metals, J. Phys. F Met. Phys. 12 (1982) 1845, https://doi.org/10.1088/0305-4608/12/8/024.
[74] J.I. Pankove (Ed.), Optical Processes in Semiconductors, Dover Publications Inc., New York, 1975.
[75] S.H. Wemple, M. DiDomenico Jr., Behavior of the electronic dielectric constant in covalent and ionic materials, Phys. Rev. B 3 (4) (1971) 1338, https://doi.org/10.1103/PhysRevB.3.1338.
[76] A.S. Hassanien, I. Sharma, Optical properties of quaternary a-$Ge_{15-x}Sb_xSe_{50}Te_{35}$ thermally evaporated thin-films: refractive index dispersion and single oscillator parameters, Optik 200 (2020) 163415, https://doi.org/10.1016/j.ijleo.2019.163415.
[77] K. Tanaka, Optical properties and photoinduced changes in amorphous as S films, Thin Solid Films 66 (1980) 271–279, https://doi.org/10.1016/0040-6090(80)90381-8.
[78] A.S. Hassanien, I. Sharma, P. Sharma, Optical and dispersion studies of thin $S_{35-x}Ge_{15}Sn_xTe_{50}$ films: assessment of some physical parameters of samples, Phys. Scr 98 (2023) 045911, https://doi.org/10.1088/1402-4896/acc2f9.
[79] R.E. Hummel, Electrons in a crystal, in: Electronic Properties of Materials, Springer, New York, 2011, pp. 63–76, https://doi.org/10.1007/978-1-4419-8164-6_6.
[80] S. Adachi, in: Properties of Semiconductor Alloys: Group-IV, III-V and II-VI Semiconductors, John Wiley & Sons Ltd., 2009, https://doi.org/10.1002/9780470744383.
[81] S. Delice, M. Isik, N.M. Gasanly, Linear and nonlinear optical characteristics of PbMoO4 single crystal for optoelectronic applications, J. Mater. Sci. Mater. Electron. 33 (28) (2022) 22281–22290, https://doi.org/10.1007/s10854-022-09006-x.
[82] E.A. Campo, Selection of Polymeric Materials—How to Select Design Properties from Different Standard, William Andrew Inc., New York, 2008.
[83] D. Sahoo, D. Alagarasan, R. Ganesan, S. Varadharajaperumal, R. Naik, Impact of irradiation doses on the structural, morphological, and linear–nonlinear optical properties of $Ge_{10}Sb_{25}Se_{65}$ thin films for optoelectronic applications, Eur. Phys. J. Plus. 137 (2022) 707, https://doi.org/10.1140/epjp/s13360-022-02930-1.
[84] A. Parida, D. Sahoo, D. Alagarasan, S. Vardhrajperumal, R. Ganesan, R. Naik, Increase in nonlinear susceptibility and refractive index in quaternary In15Sb10S15Se60 thin films upon annealing at different temperature for photonic applications, J. Alloys Compd. 905 (2022) 164143, https://doi.org/10.1016/j.jallcom.2022.164143.
[85] D.C. Sati, A. Dahshan, H.H. Hegazy, K.A. Aly, P. Sharma, Optical and optoelectronic properties of (Ge2S8)100-xTex thin films for IR optical device fabrication, Surf. Interf. 39 (2023) 102995, https://doi.org/10.1016/j.surfin.2023.102995.
[86] K.A. Aly, Y. Saddeek, Optical red shift spectra in CuxGe32S68-x films for infrared and solar cell window applications, Surf. Interf. 44 (2024) 103784, https://doi.org/10.1016/j.surfin.2023.103784.
[87] C.C. Wang, Empirical Relation between the linear and the third-order nonlinear optical susceptibilities, Phys. Rev. B 2 (6) (1970) 2045, https://doi.org/10.1103/PhysRevB.2.2045.
[88] A.N.M. Ali, N.A. Ali, S.I. Hussein, A. Hakamy, B. Raffah, A.S. Alofi, A.M. Abd-Elnaiem, Nanoarchitectonics of silver/poly (methyl methacrylate) films: structure, optical characteristics, antibacterial activity, and wettability, J. Inorg. Organomet. Polym. 33 (2023) 694–706, https://doi.org/10.1007/s10904-022-02525-4.
[89] V. Ganesh, I.S. Yahia, S. AlFaify, M. Shkir, Sn-doped ZnO nanocrystalline thin films with enhanced linear and nonlinear optical properties for optoelectronic applications, J. Phys. Chem. Solids 100 (2017) 115–125, https://doi.org/10.1016/j.jpcs.2016.09.022.
[90] H. Ticha, ˈ L. Tichý, Semiempirical relation between non-linear susceptibility (refractive index), linear refractive index and optical gap and its application to amorphous chalcogenides, J. Optoelect. Adv. Mater. 4 (2002) 381–386.
[91] Z.R. Khan, K.V. Chandekar, A. Khan, N. Akhter, M.A. Sayed, M. Shkir, H. Algarni, S. Alfaify, An impact of novel Terbium (Tb) doping on key opto-nonlinear optical characteristics of spray pyrolyzed NiO nanostructured films for opto-nonlinear applications, Mater. Sci. Semicond. Process. 138 (2022) 106260, https://doi.org/10.1016/j.mssp.2021.106260.
[92] Y. Wang, D. Sun, J. Chen, C. Shen, G. Liu, D. Wang, S. Wang, Linear and nonlinear optical characteristics effected by Na+ ions of low concentration for potassium dihydrogen phosphate crystal, Optik 251 (2022) 168481, https://doi.org/10.1016/j.ijleo.2021.168481.
[93] G. Abbady, A. Qasem, A.M. Abd-Elnaiem, Optical parameters and electronic properties for the transition of the amorphous-crystalline phase in Ge20Te80 thin films, J. Alloys Comp. 842 (2020) 155705, https://doi.org/10.1016/j.jallcom.2020.155705.